Toward the Ground-based Imaging of Satellites at Geosynchronous Altitude

D. Mozurkewich[1]
Seabrook Engineering, Seabrook MD, 20706 USA
J. T. Armstrong, R. B. Hindsley
Naval Research Laboratory, 4555 Overlook Ave, SW, Washington DC, 20375 USA
A. M. Jorgensen
New Mexico Inst. of Mining and Tech., 801 Leroy Place, Socorro, NM 87801
S. R. Restaino
Naval Research Laboratory, C/o AFRL/RDS, 3550 Aberdeen SE Albquerque NM, 87117
H. R. Schmitt
Computational Physics Inc, 8001 Braddock Rd., Springfield, VA 22151

ABSTRACT

To image satellites at geosynchronous altitude requires a telescope aperture of 50 to 200 meters, depending on the choice of wavelength and required resolution. Building such a facility is an expensive, lengthy undertaking and is probably a couple of decades away. Interferometry has been proposed as an alternative and although it looks promising on paper, so far it has failed to deliver. In the astronomical community, aperture masking – an interferometric imaging techniques – consistently produces higher-quality images than a camera with adaptive-optics. Sadly, separated-aperture interferometry lags further behind but their image quality is improving as the number of apertures increases. A bigger problem is poor sensitivity. We understand the light loss-issues and can increase the sensitivity by mitigating these problems and by using larger telescopes with adaptive optics.

In this paper, we argue for a design consisting of 30 identical telescopes mounted on a steerable boom. The telescopes feed optical fibers which in turn feed the beam combiner. We present optical and mechanical designs along with a sensitivity analysis. We discuss the applicability of this system to imaging satellites.

1 Introduction

The ability of a ground-based facility to obtain images of satellites in geosynchronous orbit is an important, though difficult requirement. Images will be useful for determining the details of a deployment failure which in turn can determine whether insurance will cover replacement costs. Color and albedo changes help diagnose on-orbit aging of components. With enough resolution, even changes in shape due to joint failures or warping due to fatigue from repeated heating and cooling cycles could be seen. Despite its importance, we know of no existing facility with enough resolution, dynamic range and sensitivity for this task.

Considering these needs, we initiated a study to design such a facility. This point design was aimed at sub-meter resolution on a 30-meter diameter satellite in geosynchronous orbit. To achieve this resolution, the diameter of the optics has to be in the 50 to 150 meter range for visible imaging and larger for the infrared. A single-optic filled-aperture is out of the question. The largest operating telescopes are 10 meters and 30-meter telescopes are being designed but these fall quite a bit short of our requirements. As a result, we considered an imaging interferometer. The exiting facilities do not have enough telescopes and do not have the required sensitivity. The field of view requires the shortest baselines to be about 2 meters at $\lambda = 0.75$ μm. This results in a packaging problem for individually steerable telescopes.

With these considerations, our point design is shown in Figure 1. Thirty telescopes are mounted on a steerable platform. Light from each of the apertures is fed to the beam combiner through equal-length, single-mode, polarization-maintaining fibers. Over a traditional ground-based interferometer, sensitivity is improved since losses due to the vacuum feed system and delay lines are eliminated. Delays are roughly equalized by pointing the platform. Fine scale fringe tracking is accomplished by stretching the fibers. Each aperture has its own adaptive optics. The beam combiner is located near the center of the platform.

[1]Send correspondence to David Mozurkewich, Seabrook Engineering 9310 Dubarry Ave, Seabrook MD 20706
E-mail: dave@mozurkewich.com

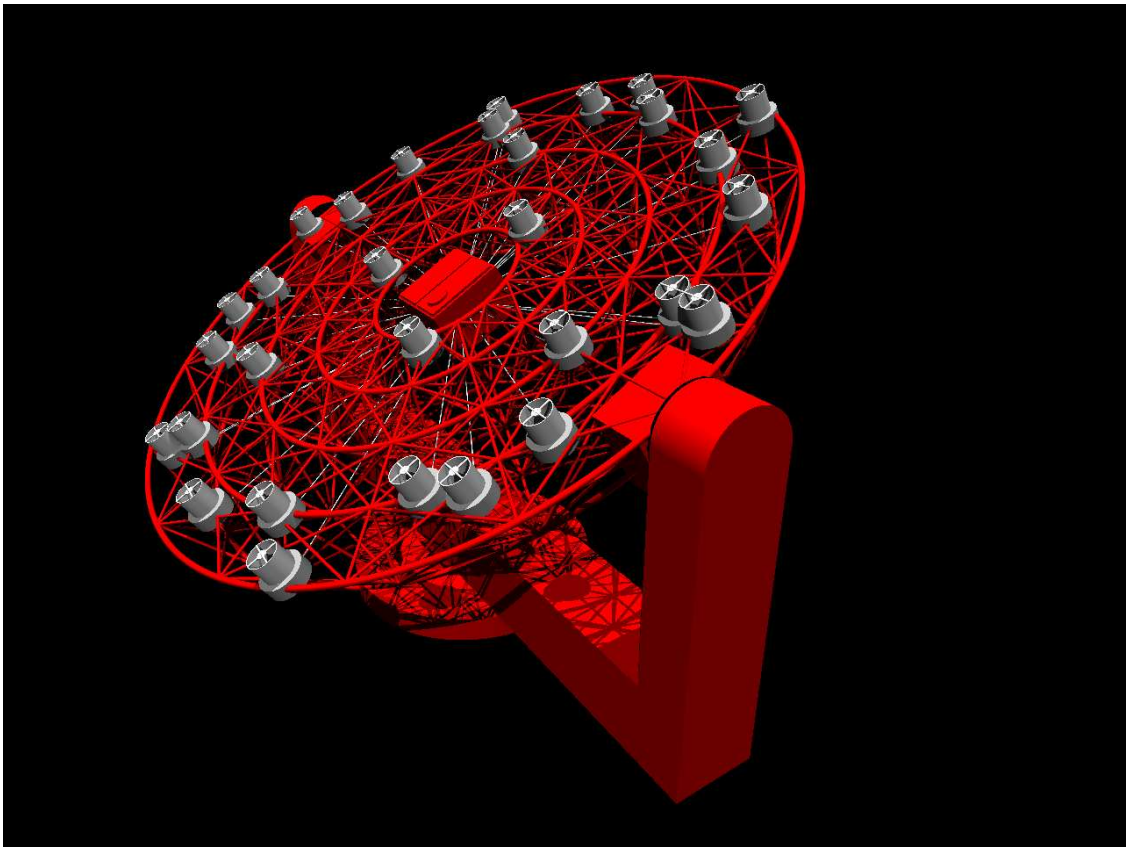

Figure 1: The concept described in this paper is an optical interferometer mounted on a steerable platform. Light from the apertures is fed to the beam combiner through equal-length, polarization-maintaining, single-mode fibers. Losses due to the vacuum feed system and delay lines are eliminated. Delays are roughly equalized by pointing the platform. Fine scale fringe tracking is accomplished by stretching the fibers. Each aperture has its own adaptive optics. The beam combiner is located near the center of the platform.

We also considered a design where all the apertures are in a line and that line is rotated about the optical axis to fill in the MTF. This one-dimensional design uses a smaller structure and fewer apertures. However, it takes longer to make an image; the two-dimensional design seems to be a better choice if speed of imaging is a design driver. Long imaging times may be problematic due to the changing solar illumination angle on time scales of an hour.

Detailed imaging simulations achieved a resolution of 0.3 meters with good dynamic range. See Schmitt et al(2011)[1] for details. We chose a visible magnitude of 13.5 and colors based on Sanchez et al (2000)[2]. The design is a passive imaging system and is scalable; increasing the resolution by a factor of 5 requires a bigger structure and more telescopes but no new technology. It is always difficult to estimate sensitivity of a complicated optical system. We have one, perhaps two, magnitudes of reserve. Beyond that, we need more collecting area and, perhaps, active systems such as laser beacons.

2 Detailed Design

For a ratio of longest to shortest baseline of 30 and a non-redundant configuration, we need approximately 30 apertures in the interferometer. One possible configuration for the apertures is shown in Figure 2. The apertures are placed on an hexagonal grid. The arrangement shown is the most-compact, non-redundant configuration with 30 apertures.

The optical train is shown in Figures 3 and 4 and the parameters collected in Table 1. The design

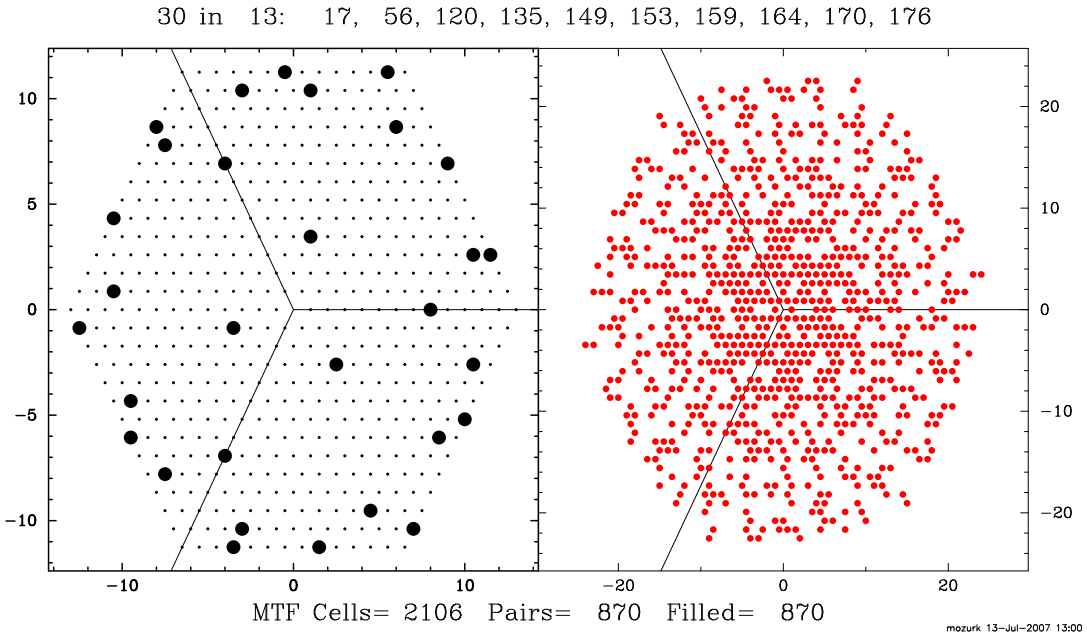

Figure 2: The proposed configuration for the apertures. This is a 30-element, non-redundant array.

incorporates an unusually small secondary in order to keep light loss from the central obscuration to less than 2%. The third mirror, M_3, is off-axis and transfers the turbulence layer onto the deformable mirror. Because, this system needs a very small field of view, performance should not depend strongly on the choice of the turbulence distance. For this design, it was assumed to be 20 meters above the primary but changing that distance has only a very small effect on the focal length of M_3.

The dichroic, D_1, picks off the light (either visible or J band) for wavefront sensing while, D_2 divides the remaining light between the imaging and fringe tracking interferometers. The interferometric bands consist of atmospheric dispersion compensation optics, A, and a lens which focuses light onto the fiber. The wavefront sensing arm replaces the fiber with a microlens array which divides the aperture for a Shack-Hartmann sensor. The two interferometry channels also contain a linear polarizer, P, needed to avoid interferometry problems caused by the the birefringence of the polarization maintaining fibers.

The imaging beam combiner is shown in Figure 4. The optical fibers from the telescopes enter the system at F where a microlens array collimates the beams. The fibers are in a column perpendicular to the plane of the figure. An optional polarizer, P, cleans up the beams M_5 is an off-axis parabola that forms overlapping images of all the fiber tips. These images are azimuthally symmetric with a Gaussian radial intensity profile. All fringes are present in this image. The lens L_2, with the help of two fold mirrors, F_1 and F_2, scale this image to match the detector at D.

The second lens, L_3, is cylindrical, is orientated so that it has no power in the plane of the figure and forms an image of the microlens array on the detector. This compresses the otherwise azimuthally-symmetric image into a thin strip. The fringes vary along the strip. A prism or other dispersing element, can be inserted as shown between L_2 and F_2. The detector now has fringe information in one direction and spectral information in the perpendicular direction. A second function of this lens is to separate different columns at F into different columns at D. This provides important flexibility in the choice of which fringes are observed. See Mozurkewich and Traore[3] for a more detailed description of this beam combiner and its performance.

Table 1: Optical parameters for the layout shown in Figure 3

Optic	Description		
M_1	primary	D=1400 mm,	f=2000 mm
M_2	secondary	D=140 mm,	f= -221 mm
M_3	tertiary	D= 5 mm,	f= 72 mm
DM	deformable mirror	D=5 mm,	
L_1	fiber feed	D=7 mm,	f= 34 mm
M_5	Combiner Primary	D=75 mm,	f=1000 mm
L_2	Relay Lens	D=250 mm,	f= 50 mm
L_3	Cylindrical Lens	D=150 mm,	f= 50 mm
r_0	Fried parameter, 0.5μm	150 mm	
t_0	Coherence time, 0.5μm	3.0 mS	
η_{WFS}	Throughput, WFS	0.4	
η_I	Throughput, interferometry	0.1	
WFS	Bandpasses μm	$\lambda_0 = 0.5$,	$\Delta\lambda$ =0.2
Fringe Tracking	Bandpasses in μm	$\lambda_0 = 1.6$,	$\Delta\lambda$ =0.3
Imaging	Bandpasses in μm	$\lambda_0 = 0.75$,	$\Delta\lambda$ =0.3

Table 2: Throughput estimate

Optic	WFS	R	H
M_1	.98	.98	.98
M_2	.98	.98	.98
M_3	.98	.98	.98
DM	.95	.95	.95
D_1	.80	.85	.90
D_2		.90	.90
M_3			.98
A	.96	.96	.96
Lens_1	.96	.96	.96
WFS	.90		
Polarizer		.50	.50
Fiber Coupling		.80	.80
Fiber Throughput		.96	.96
μ lens array		.90	.90
Polarizer 2		.90	.90
Primary		.98	.98
Pinhole		.80	.80
Fold 1		.98	.98
magnification lens		.96	.96
prims		.96	.96
Fold 2		.98	.98
cylindrical lens		.96	.96
detector QE	0.80	.80	.80
total throughput	0.47	0.105	0.108

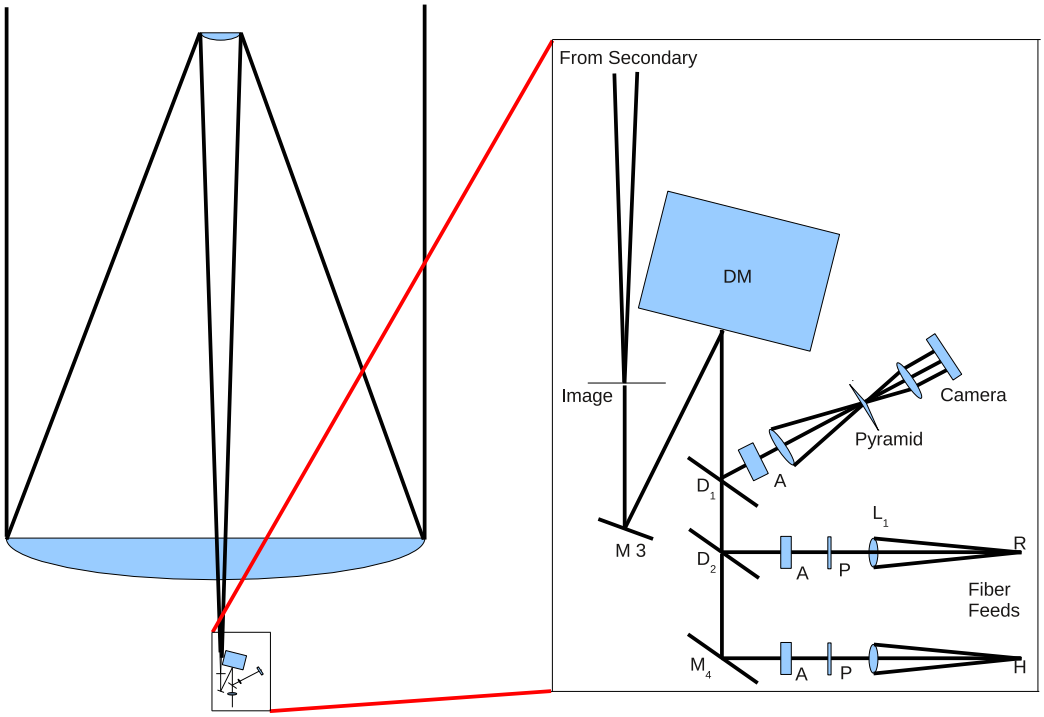

Figure 3: Optical layout of an aperture (to scale) for the 1.4 meter system. There are six optics between the sky and the optical fiber. The third powered optic is needed to image the turbulence above the telescope onto the deformable mirror(DM). Next, a pick-off beam splitter delivers light to a pyramid wavefront sensor while the remaining light is divided into two bands for interferometry. Both bands are focused onto optical fibers. In this design, the turbulence is assumed to be 20 meters in front of the primary. That distance can be changed by using a different focal length for M_3 and changing the separation of M_3 and the DM.

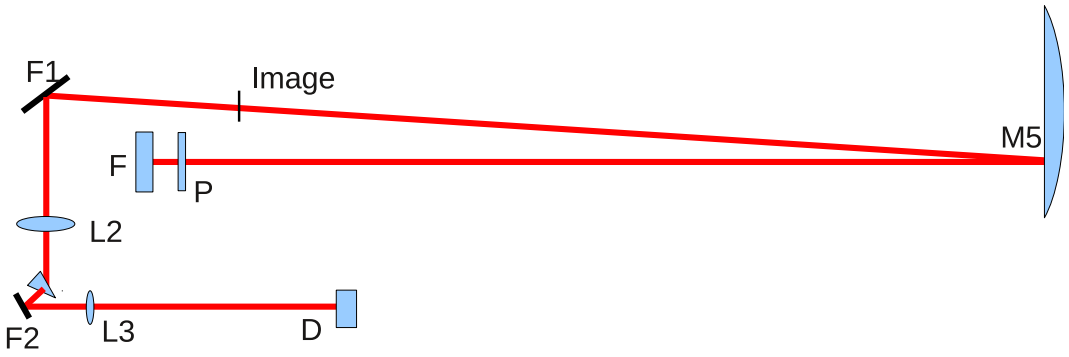

Figure 4: Optical layout of the beam combiner (roughly to scale). As designed, this system can handle up to 90 input beams. With fewer apertures, more spectral resolution is possible. Details in the text.

3 Wavefront Sensing

Our first tasks is to choose a bandpass for wavefront sensing. We follow the calculation presented in Mozurkewich et al[4]. To summarize, the wavefront variance, in radians^2, is

$$\sigma^2 = 0.0449 + 1.261 N^{-0.45} \tag{1}$$

where $N = nr_0^2 t_0$ is the number of detected photons per coherence volume, that is per area r_0^2 in time t_0. This is plotted in Figure 5 for the five bandpasses we consider. The upper panel shows the expected flux from the satellite. The second panel shows N, where r_0 and t_0 were scaled as $\lambda^{1.2}$. The third panel shows σ from Equation 1. To compare performance at different wavelengths, σ is multiplied by $\lambda/2\pi$ and shown in the lower panel. In each panel, the circles are for a typical satellite brightness, $V = 13.5$, the X's mark the results for a target two magnitudes fainter. Both sets of calculations assume typical satellite colors: $(V-I) = 1.1$, $(V-J) = 2.8$, $(V-H) = 3.3$ and we assumed, $(V-K) = 3.3$. Since there is not much difference in performance between the spectral bands, we chose the shortest wavelength band, 0.5μm for wavefront sensing.

4 Fringe Tracking

The signal to noise for a single baseline in a fringe tracker observing an unresolved source is given by

$$SNR_{FT} = \frac{2}{\pi k}\sqrt{kN_{FT}} \tag{2}$$

$$N_{FT} = \eta_{FT} e^{-\sigma^2} \frac{\pi D^2}{4} t_{FT} n \tag{3}$$

where k is the number of apertures combined, N_{FT} is the number of photons per integration per telescope reaching the fringe detector, η_{FT} is the throughput of the interferometer for a perfect wavefront, σ^2 is the wavefront variance, at the interferometer wavelength at the input to the single mode optical fiber, D is the diameter of the telescope and $t_{FT} = 2t_0$ is the interferometric integration time. The wavefront variance contains two terms, the WFS variance and a constant term due to static optical aberrations.

For an unresolved source, the two beam combiner designs shown work equally well; the combiner with large k has a lower signal to noise per baseline but simultaneously observes more baselines. For observing resolved sources, only the short baselines have significant fringe amplitude and combiners with smaller k perform better.

These calculations are shown in Figure 6. Again, circles and x's are for a mean satellite and a faint satellite. There are two SNR curves for for each satellite. The upper curve is for a pairwise ($k = 2$) combiner while the lower curve is for a $k = 15$ aperture combiner. A science combiner requires a large value of k but for a fringe tracker may work with a fairly small k. The telescope diameter was chosen to give $SNR = 5$ for the fainter satellite.

The choice of H-band or K-band for fringe tracking is difficult. The visibility amplitude will be higher at the longer wavelength. This will improve signal to noise but it will also be more difficult to transfer that phase to the imaging wavelength. For the remainder of this paper, we will adopt H band fringe tracking.

5 Imaging Interferometry

The Imaging Interferometer is operated at a wavelength of 0.75μm, the shortest unused wavelength. It is similar to the fringe tracker with one major exception: many of the baselines are assumed to have low fringe amplitudes and therefore the signal to noise of individual data frames is too low to be useful. The signal to noise is increased by coherently adding together many frames using phases predicted from the fringe tracker. The phase predictions from the fringe tracker are not perfect and therefore the visibility amplitude of the imaging data is reduced by $e^{-\sigma_{FT}^2}$ where σ_{FT} is the uncertainty of the imaging interferometer phase, in radians, as predicted by the fringe tracker. The resulting signal to noise of the imaging interferometer is

$$SNR_I = \frac{2e^{-\sigma_{FT}^2}}{\pi k}\sqrt{kN_I} \tag{4}$$

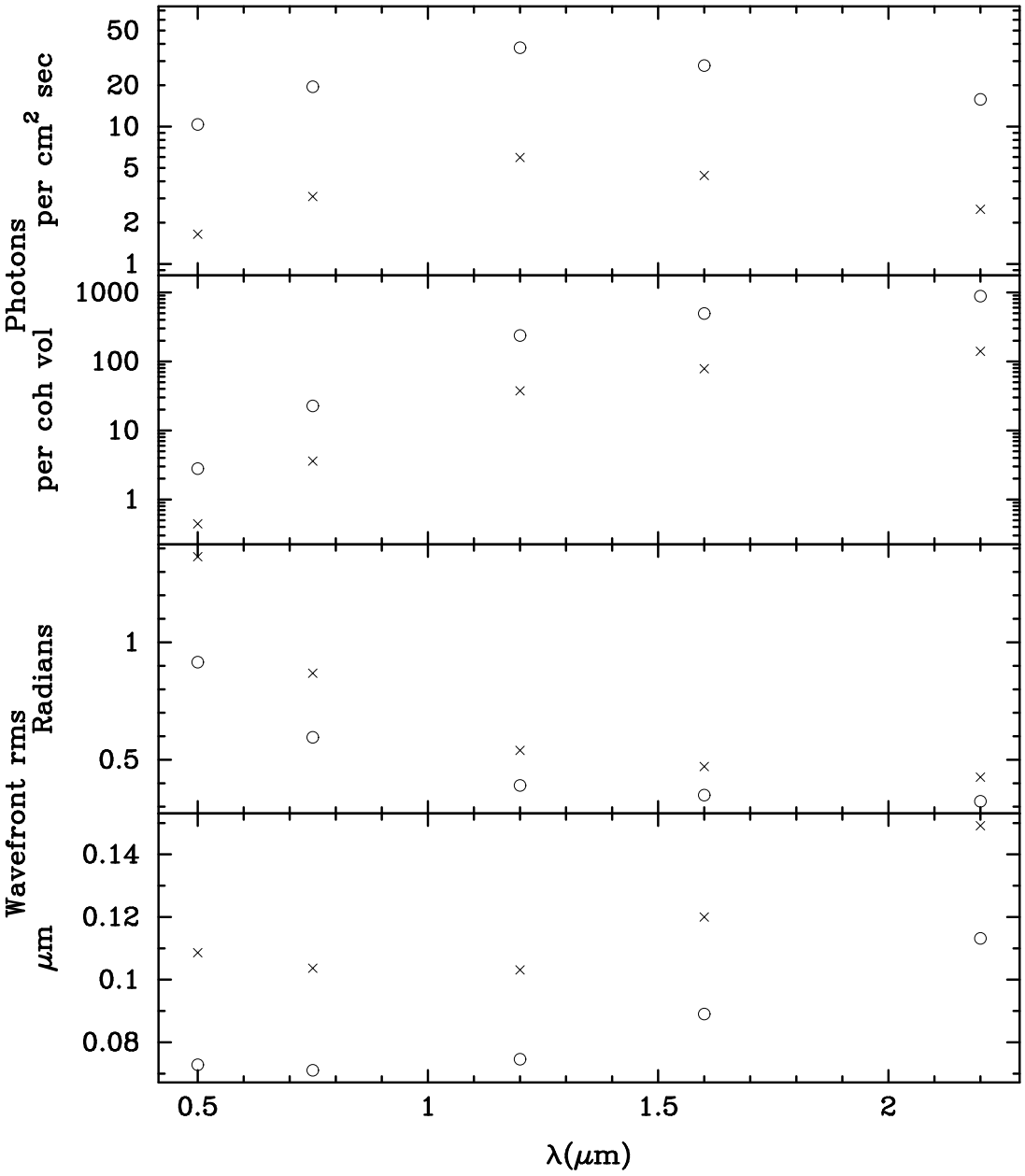

Figure 5: Wavefront sensor sensitivity versus wavelength band. The circles are for a typical satellite brightness of $V = 13.5$ and typical colors (given in the text). The x's indicate a satellite two magnitudes fainter. Details are described in the text but as expected, the shortest wavelengths give the best performance.

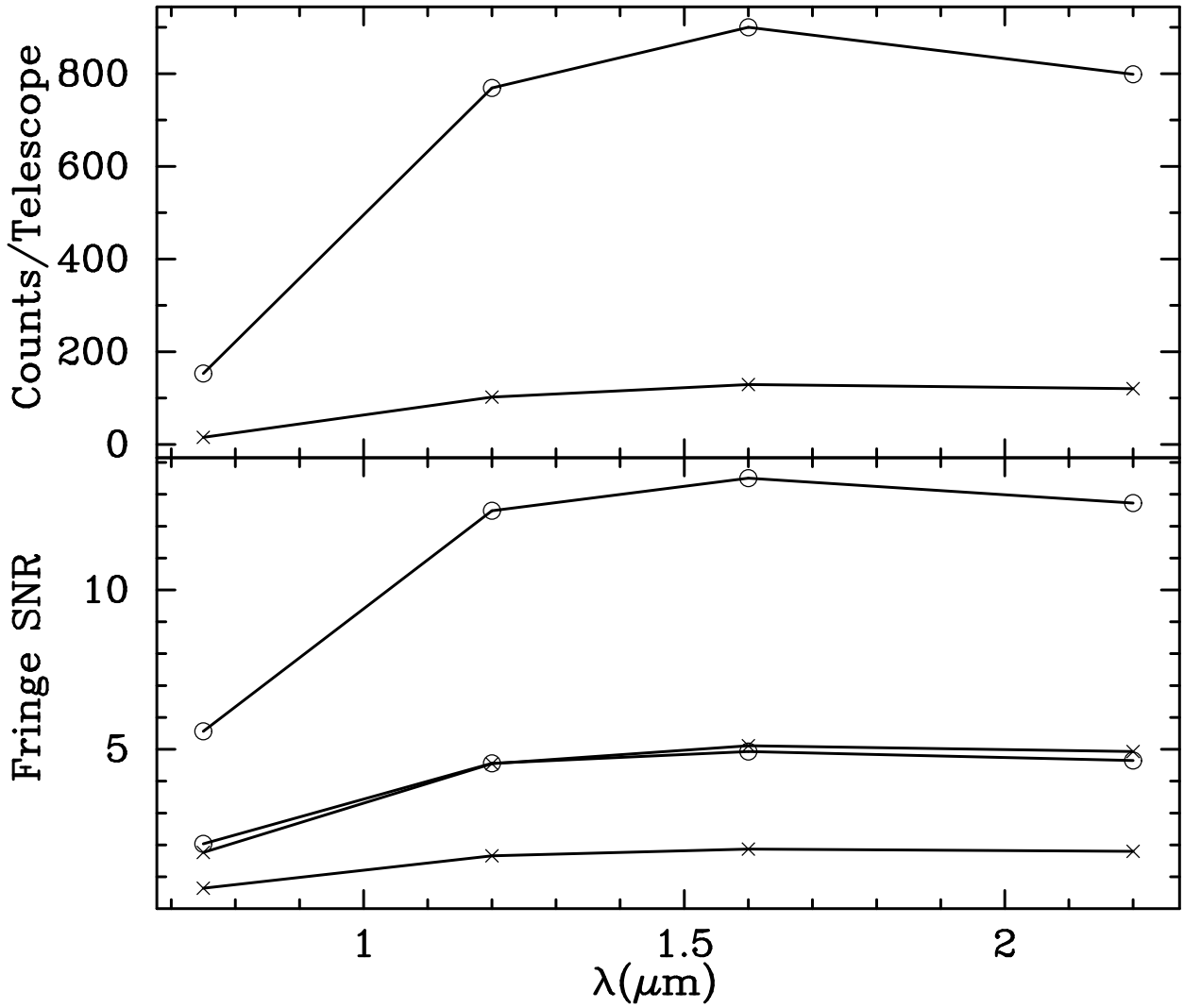

Figure 6: This figure shows the signal-to-noise of an interferometer as function of wavelength. The wavefront sensor is the V-band system described in Figure 5. As in that figure, the circles and x's correspond to mean ($V = 13.5$) and faint ($V = 15.5$) satellites. The upper panel shows the number of detected photons per integration per aperture. The lower panel explores the fringe signal to noise. Two cases for each satellite are shown. The upper curves are for a two-beam interferometer. The lower curves are for one baseline of a fifteen beam all-on-one combiner.

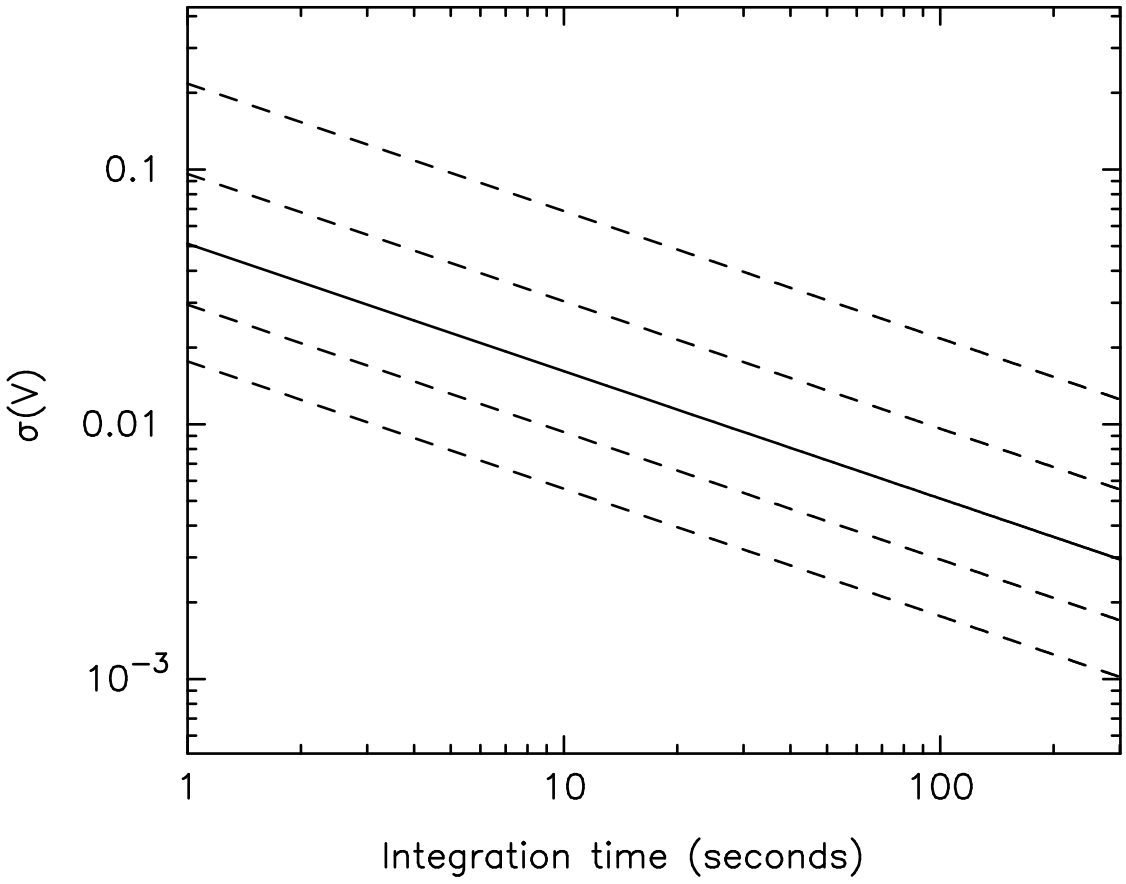

Figure 7: This plot shows the visibility uncertainty as a function of integration time. The solid line is for the median satellite spectrum; the dashed lines to either side show the results for the same spectrum but one and two magnitudes brighter or fainter.

$$N_I = \eta_I e^{-\sigma_I^2} \frac{\pi D^2}{4} t_I n \tag{5}$$

Figure 7 shows this result. Here, $k = 15$. The solid line is the satellite with mean brightness, the dashed lines show integration times for satellites that are one or two magnitudes brighter or fainter than the mean. In all cases, reasonable performance is achieved with integration times of a few hundred seconds.

6 Summary

The result of this study is not intended to be a final design but rather a demonstration that this approach to imaging satellites in geosynchronous orbit is worth pursuing. The sensitivity is sufficient and image quality simulations (presented in [1]) show that 30 telescopes, as assumed here will provide good image quality. The biggest hole is this work is the assumption of unit fringe visibility on the shortest baselines (needed to phase the array). That problem is partially addressed here by using longer wavelengths (1.6 μm) for phasing the array then for imaging (0.7 μm). A more detailed investigation of this problem has been started in [5]. Using more telescopes to reduce the baseline length needed for phasing or increasing the diameter of the telescopes are both viable solutions if that study shows more sensitivity is needed.

Some this work was supported by NASA contracts NNX07CA49P and NNX08CA21C, Seabrook Engineering IRAD, NLR 6.1 base funding, the Office of Naval Research and the Oceanographer of the Navy.

References

[1] H. R. Schmitt, D. Mozurkewich, S. R. Restaino, J. T. Armstrong, R. B. Hindsley, and Jorgensen, Anders M. , "Simulated optical interferometric observations of geostationary satellites," in *Society of Photo-Optical Instrumentation Engineers (SPIE) Conference Series*, *Society of Photo-Optical Instrumentation Engineers (SPIE) Conference Series* **8165A**, 2011.

[2] D. J. Sanchez, S. A. Gregory, D. K. Werling, T. E. Payne, L. Kann, D. M. Finkner, L. G. Payne, and C. K. Davis, "Photometric measurements of deep space satellites," in *Society of Photo-Optical Instrumentation Engineers (SPIE) Conference Series*, *Society of Photo-Optical Instrumentation Engineers (SPIE) Conference Series* **4091**, 2000.

[3] D. Mozurkewich and A. Traore, "Beam combination with a large number of apertures," in *Society of Photo-Optical Instrumentation Engineers (SPIE) Conference Series*, *Society of Photo-Optical Instrumentation Engineers (SPIE) Conference Series* **7734**, July 2010.

[4] D. Mozurkewich, S. R. Restaino, J. T. Armstrong, and G. C. Gilbreath, "Adaptive optics performance model for optical interferometry," *Applied Optics* **46**, pp. 4413–4422, 2007.

[5] A. M. Jorgensen, "," in *These proceedings*, *AMOS* **2011**, 2011.